The interpretation of a long-standing rheological flow problem using computational rheology and a PTT constitutive model

I.E. Garduño , H.R. Tamaddon-Jahromi , K. Walters , M.F. Webster

PII: S0377-0257(15)00205-0
DOI: 10.1016/j.jnnfm.2015.12.004
Reference: JNNFM 3723

To appear in: *Journal of Non-Newtonian Fluid Mechanics*

Received date: 13 June 2015
Revised date: 4 December 2015
Accepted date: 11 December 2015

Please cite this article as: I.E. Garduño , H.R. Tamaddon-Jahromi , K. Walters , M.F. Webster , The interpretation of a long-standing rheological flow problem using computational rheology and a PTT constitutive model, *Journal of Non-Newtonian Fluid Mechanics* (2015), doi: 10.1016/j.jnnfm.2015.12.004

Highlights

- The rotation of a solid sphere in an non-Newtonian elastic liquid is considered.
- Under some conditions a secondary flow is predicted with the Giesekus model.
- Moving away from the restriction of slow flow, the inertial vortex flow can be also predicted by the PTT model.

The interpretation of a long-standing rheological flow problem using computational rheology and a PTT constitutive model

I.E. Garduño[a], H.R. Tamaddon-Jahromi[a], K. Walters[b], M.F. Webster[a†]

[a] *Institute of Non-Newtonian Fluid Mechanics*, Swansea University Bay Campus, College of Engineering, Fabian Way, Swansea, SA1 8EN, UK
[b] *Institute of Mathematics, Physics and Computer Science*, Aberystwyth University, Aberystwyth, SY23 SBZ, UK

Abstract

Modern Computational Rheology techniques are used to interpret an experimental observation, which has remained unresolved for over four decades. The simple flow in question involved the rotation of a solid sphere in an infinite expanse of non-Newtonian elastic liquid. Under *some* conditions, Giesekus observed an interesting secondary flow. This added an 'inertial' secondary flow near the rotating sphere to the well-understood 'slow-flow' features observed and predicted by others in the 1960s. By employing a Phan-Thien/Tanner (PTT) constitutive model and moving away from the restriction of 'slow-flow', we show that it is possible to predict numerically the inertial vortex observed by Giesekus.

Keywords: rotating sphere, secondary flow field, Giesekus inertial vortex, hybrid finite element/finite volume scheme, PTT model

1. Introduction

The flow we wish to understand and interpret is discussed in the "Rheological Phenomena in Focus" book written by Boger and Walters [1]. Briefly, when a solid sphere is rotated in an infinite expanse of elastic liquid, interesting secondary-flow patterns are generated depending on the relative strengths of fluid inertia and viscoelasticity. In Figure 1 (upper-row), we show a typical schematic representation of the secondary flow initially provided by Thomas and Walters [2]. In the first instance, the flow in Type 1 is dominated by inertia, whilst in Type 3 viscoelasticity dominates. Finally, Type 2 shows an intermediate state, where fluid inertia and viscoelasticity are both prominent.

The 1960s literature contains examples where experimental data were able to confirm the theoretical predictions (see, for example, [3]). However, Giesekus [4], in an experimental paper written somewhat later in 1970, demonstrated that other flow fields were possible, depending on the fluids under study and the rotational speed of the sphere.

The flow of interest in the present work is shown in Figure 2 (see [1, 4]). This was obtained for a 1.3% solution of polyisobutylene in decalin. Here, there is an outer inertial zone (not highlighted by the dye-injection technique) and also an inner inertial zone, separated by a viscoelastic zone. Boger and Walters [1] emphasize that the inner inertial zone is an elusive

† Corresponding Author: m.f.webster@swansea.ac.uk

phenomenon to capture! It is this feature, which we wish to study and predict in the present work. In the process, we shall alight (without comment) on other secondary-flow features that are not included in the slow-flow second-order theory. Interestingly, as we have already suggested, the 1970s *experimental* study of Giesekus [4] also includes a range of other phenomena not predicted by the second-order theory.

2. Previous work

Consider a steady simple shear flow with Cartesian velocity components given by

$$\mathrm{v_x} = \dot{\gamma}\mathrm{y}, \quad \mathrm{v_y} = \mathrm{v_z} = 0, \tag{1}$$

where $\mathrm{v_i}$ is the velocity component and $\dot{\gamma}$ is the constant shear rate. The associated stress field is usually written in the form:

$$\begin{aligned} &\sigma_{xy} = \sigma = \dot{\gamma}\ \eta(\dot{\gamma}), \\ &\sigma_{xx} - \sigma_{yy} = N_1(\dot{\gamma}) = \Psi_1 \dot{\gamma}^2, \\ &\sigma_{yy} - \sigma_{zz} = N_2(\dot{\gamma}) = \Psi_2 \dot{\gamma}^2. \end{aligned} \tag{2}$$

Here, σ is the shear-stress, η is the shear viscosity and N_1 and N_2 are the first and second normal stress-differences, respectively. In a uniaxial extensional flow, one may define the extensional viscosity η_e, with dependency on the constant extensional strain rate $\dot{\varepsilon}$:

$$\mathrm{v_x} = \dot{\varepsilon}\mathrm{x}, \quad \mathrm{v_y} = -\frac{\dot{\varepsilon}\mathrm{y}}{2}, \quad \mathrm{v_z} = -\frac{\dot{\varepsilon}\mathrm{z}}{2}, \tag{3}$$

$$\sigma_{xx} - \sigma_{yy} = \sigma_{xx} - \sigma_{zz} = \dot{\varepsilon}\eta_e(\dot{\varepsilon}). \tag{4}$$

For the sufficiently slow flow of relevance in the theoretical work of Thomas, Walters and Waters [2, 5], $\eta = \eta_0 - \eta_2 \dot{\gamma}^2$ and Ψ_1 and Ψ_2 are material constants. We note that on theoretical grounds N_1 must be positive and N_2 is usually found to be relatively small and negative from experiments. The viscoelastic parameter *m*, in the work of Thomas, Walters and Waters [2, 5], is given by

$$m = \left[N_1 - 2N_2\right] \Big/ \left(2\rho a^2 \dot{\gamma}^2\right) = \left[\Psi_1 - 2\Psi_2\right] \Big/ \left(2\rho a^2\right). \tag{5}$$

We would anticipate *m* to be positive for most, if not all, elastic non-Newtonian liquids. The material parameter *m* can be reinterpreted through non-dimensional numbers as $m = (Wi/Re)(1-\beta)$ where the Weissenberg number is $Wi = \lambda_1 U / L_{\text{sphere}}$, the Reynolds number is defined as $Re = \rho a U / \eta_0$, and β is the solvent ratio (defined below). Additionally, λ_1 is defined as the relaxation time, U is the characteristic velocity, L_{sphere} the characteristic length, ρ is the fluid density, a is the sphere-radius and η_0 is the zero-shear total viscosity.

We shall now consider the flow generated by the slow rotation of a solid sphere of radius *a* in an infinite expanse of elastic liquid. Using the obvious spherical polar coordinate system and introducing an appropriate stream function χ_1 and couple *C*, it is possible to derive general formulae *for sufficiently slow-flow* in terms of parameter *m* :

$$\chi_1 = \frac{(r_1-1)^2}{8r_1^3}\left[(1-4m)r_1 - 8m\right]\sin^2\theta\cos\theta, \tag{6}$$

where $r_1 = r/a$, and the couple *C* on the sphere is given by

$$C = 8\pi\eta_0\Omega a^3\left[1 + L\left(\frac{1}{120} + \frac{m}{140} - \frac{2m^2}{15} - \frac{12\sigma_c}{5}\right)\right]. \tag{7}$$

The parameter σ_c can be expressed in the form $\sigma_c = \eta_0\eta_2/\rho^2 a^4$. The formulae involve a non-dimensional parameter *L (related to the Reynolds number)*:

$$L = \left(\frac{\Omega a^2}{\nu}\right)^2 = \left(\left[\Omega a\right]\left[\frac{a}{\nu}\right]\right)^2 = \left([U_{\text{sphere}}]/[U_{\text{material}}]\right)^2 = Re^2. \tag{8}$$

Here, $\nu = \eta_0/\rho$ is the kinetic viscosity, Ω is the base-reference rotational speed of the sphere (Ω_{sphere}), so that $U_{\text{sphere}} = a\Omega_{\text{sphere}}$, and $U_{\text{material}} = \nu/a$ is a counterpart base-reference viscous material velocity scale. In particular, one notes that the ratio of the two independent velocity scales equates to the Reynolds number.

In the present paper, we shall concentrate on the stream function χ_1, which for slow flow, as we have indicated, has the amazingly simple form given by eq. (6) (see, for example, [5]). Referring to Figure 1 and eq. (6), it is a simple matter to associate Type 1 behaviour with $0 \le m \le 1/12$, Type 2 behaviour with $1/12 < m < 1/4$, and Type 3 behaviour with $m \ge 1/4$ (see, for example, [2, 5]). We emphasize again that the simple stream function (equation 6) is valid for all elastic liquids, provided the flow is slow enough for second-order terms in *L* to be neglected. We see that Type 2 flow can be split into two regions separated by a spherical interface. The theory provided in [2] defines the radius of the interface as

$$r_1^* = \frac{8m}{1-4m}. \tag{9}$$

Equation (9) provides a simple relationship between the rheological properties of the fluid medium and the radius of the secondary flow cell. In [2], the theory also presented a functional relationship for the distance between a nodal point and the centre of the sphere, which is related to *m*, via

$$r_1^{(n)} = 12m, \tag{10}$$

$$\theta^{(n)} = \sin^{-1}\left(\left(\frac{2}{3}\right)^{\frac{1}{2}}\right) = 54^{\circ}\,44'. \tag{11}$$

In the 1960s, significant attention was paid to the flow under discussion (see, for example, [2, 3, 5]). It is probably true to say that some of the theoretical work could have been avoided, if it had been realized at the time that, for slow-flow, the 'order' equations of Coleman and Noll [6] provide complete generality for the simulation of the secondary-flow fields shown in Figure 1 (see, for example, [5]). However, as we have already implied, the experimental work of Giesekus [4] in 1970 opened up a new chapter, which required a shift away from the relative simplicity of the earlier second-order slow-flow theory. Theoretical attempts to move away from the second-order slow-flow analyses of the 1960s were made by Fosdick and Kao [7] and Williams [8]. However, the relevant analyses did not address the particular problem highlighted in the present paper. So, in the present work, we choose to employ a popular constitutive model to address the problem. There is a degree of choice here, but we have chosen to employ the popular Phan-Thien/Tanner (PTT) model [9], named after the two authors of the original paper (Nhan Phan-Thien and Roger Tanner). Our basic aim is simply to show that modern computational techniques, used in conjunction with a popular constitutive equation (which is not restricted to 'slow-flow'), can predict one of the main unresolved features of the Giesekus experiments.

3. Flow problem specification and the PTT model

For incompressible viscoelastic flow under isothermal conditions, the governing equations are those for mass balance (continuity), linear momentum transfer, together with an appropriate constitutive model.

The mass balance equation is expressed as

$$\nabla \cdot u = 0, \tag{12}$$

and the linear momentum transfer equation as

$$Re\left(\frac{\partial u}{\partial t} + u \cdot \nabla u\right) = -\nabla p + \nabla \cdot \mathrm{T}, \tag{13}$$

coupled with an equation of state for the stress (T). Here, the notation implies that u is the fluid velocity (vector field), p the isotropic fluid pressure, ∇ is a spatial differential operator (over spatial variable **x**) and t represents the independent variable time. We decompose the appropriate extra-stress tensor (T) into two, viscous and polymeric, parts viz.

$$\mathrm{T} = \mathrm{T}^{(1)} + \mathrm{T}^{(2)}. \tag{14}$$

with the solvent (Newtonian) stress contribution $\mathrm{T}^{(1)}$ defined as $\mathrm{T}^{(1)} = 2\beta \mathrm{d}$.

The constitutive equation for the Phan-Thien/Tanner (PTT) [9] model we have employed provides the following expression for the polymeric extra-stress $\mathrm{T}^{(2)}$:

$$Wi\overset{\square}{T}^{(2)} = 2\left(1-\beta\right)\mathrm{d} - f\mathrm{T}^{(2)}, \tag{15}$$

where $\overset{\square}{T}^{(2)} = \left(1-\frac{\xi}{2}\right)\overset{\nabla}{T}^{(2)} + \frac{\xi}{2}\overset{\Delta}{T}^{(2)}$ represents a linear (Gordon-Schowalter) combination of the upper-convected (contravariant) and lower-convected (covariant) time derivatives, defined as:

$$\overset{\nabla}{T}^{(2)} = \frac{\partial T^{(2)}}{\partial t} + u\cdot\nabla T^{(2)} - \nabla u^{\dagger}\cdot T^{(2)} - T^{(2)}\cdot\nabla u,$$
$$\text{and}\quad \overset{\Delta}{T}^{(2)} = \frac{\partial T^{(2)}}{\partial t} + u\cdot\nabla T^{(2)} + \nabla u^{\dagger}\cdot T^{(2)} + T^{(2)}\cdot\nabla u. \tag{16}$$

Here, the rate of deformation tensor, $\mathrm{d} = (\nabla u + \nabla u^{\dagger})/2$, and the viscosity solvent-fraction parameter β is defined as $\beta = \eta_{solv}/\left(\eta_{solv} + \eta_{poly}\right)$, where one identifies $\eta_{solv} = \eta_0\beta$ and $\eta_{poly} = \eta_0\left(1-\beta\right)$ as solvent and polymeric solute viscosity components, respectively.

In the present context, a truncated Linearized PTT version (the *so-called* LPTT model) is used, where the *f* functional is represented through a linear function of the trace ($\mathrm{T}^{(2)}$):

$$f = 1 + \frac{\varepsilon Wi}{1-\beta}Tr\left(\mathrm{T}^{(2)}\right). \tag{17}$$

Then, the corresponding rheometrical functions for the LPTT model are given by:

$$\eta_s = \beta\eta_0 + \frac{\eta_0\left(1-\beta\right)}{f},$$
$$N_1 = \frac{2\eta_0\left(1-\beta\right)\lambda_1\dot{\gamma}^2}{f^2},$$
$$N_2 = -\frac{\eta_0\left(1-\beta\right)\lambda_1\dot{\gamma}^2\xi}{f^2},$$
$$\eta_e = 3\beta\eta_0 + 3\eta_0\left(1-\beta\right)\left[\frac{f}{f^2 - f\lambda_1\dot{\varepsilon} - 2\lambda_1^2\dot{\varepsilon}^2}\right]. \tag{18}$$

As we see in Figure 3, such an LPPT model manifests a weakening on N_1 and a finite extensional viscosity, which is effectively controlled by the material parameter (ε). A second material parameter (ξ) modifies the shear-viscosity and the second normal stress-difference coefficient. As such, these two model parameters ε and ξ, may be employed to control, as desired, the prescribed extensional and shear response of the model. In steady shear flow, the ratio between the normal stress-differences is $N_2/N_1 = -\xi/2$. Hence, the non-zero material parameter ξ may be associated with stronger second normal stress-difference effects, see Figure 3. Typically, Phan-Thien and Tanner [9] suggested using $\xi = 0.2$ for LDPE. However, the material parameter is mathematically defined and is valid for $0 \le \xi \le 2$. Note that, the

value of *m* we shall use in the PTT model is given by the 'slow-flow' formula provided by eq. (5) (see Garduño et al. [19]).

Additionally to avoid ambiguity and to complete the problem formulation, the rotation of the sphere is achieved through a constant angular velocity Ω_{sphere}, about an axis of rotation into the vertical plane. The coordinate system is chosen in such a way that its origin is located at the centre of the sphere.

In the original 1960 – 1970 rotating-sphere experiments, a thin vertical rod was used to rotate the sphere (see, for example, Figure 8.3 in [24]). The resulting experiments indicated that there was effectively symmetry about the obvious horizontal plane, intersecting the horizontal central plane through the sphere, showing clearly that the rotating rod had little influence on the overall flow patterns. This provided a justification for ignoring the rotating rod in the early theoretical analyses, as likewise in the bulk of the present numerical simulation work.

The symmetric nature of the problem allows representation in a single quadrant of the $(r,\ \theta)$-polar plane. The boundary conditions are established over the four different boundaries. First, no-slip is established over the sphere surface; here, only rotational velocity $(\Omega_{\text{sphere}} a\sin\theta)$ is non-zero, imposed as anti-clockwise into the plane (viewed from above); whilst symmetry conditions are applied on the polar-equatorial axes (with vanishing shear stress). Additionally, it is assumed that the containing vessel has infinite outer dimensions, implying that at larger distance away from the sphere, the fluid is to all intent and purposes at rest.

The quadrant boundary conditions for this problem are defined through the velocities on the sphere itself, the two axes, polar and equatorial, and the far-field boundary. These are given as standard (see Thomas and Walters [2]) in the spherical quadrant of interest. Corresponding velocity components $(U^{\rho}, V^{\theta}, W^{\phi})$, must satisfy the stream function (eq. 6) and the boundary conditions at the sphere surface, so that with $r_1 = r/a$:

$$V^{\theta} = \frac{\nu}{a} u_2^{\theta} = \frac{\nu}{a} \frac{(r_1 - 1)}{4 r_1^5} (r_1 - 12m) \sin\theta \cos\theta. \tag{19}$$

And on the sphere,

$$W^{\phi} = \Omega_{\text{sphere}} a u_3^{\phi} = \Omega_{\text{sphere}} a \sin\theta, \tag{20}$$

from which appropriate non-dimensional velocity components $(u_1^{\rho}, u_2^{\theta}, u_3^{\phi})$ may be extracted. These expressions are linked to a specific value of the parameter *m*, which implies that the initial conditions proceed from these computations. Then, Ω_{sphere} is defined as a base-reference *angular velocity* of the sphere, and $U_{base-ref} = \nu/a$ as a base-reference viscous *material velocity-scale*. In addition, θ is the angle measured from the vertical axis of rotation, with orientation taken on the vertical polar-axis as $(\theta = 0^{\text{o}})$ and on the equatorial-axis $(\theta = 90^{\text{o}})$. Note in particular, the use of the dual scales on velocity components of Thomas and Walters [2], who used $(U_{\text{sphere}} = \Omega_{\text{sphere}} a)$ for (u^{ϕ}) as a sphere rotational velocity-

scale, and $U_{\text{material}} = (\nu/a)_{base-ref}$ for (u^{ρ}, u^{θ}) as a viscous material velocity-scale. These dual velocity-scales imply that two independent controlling influences apply in this problem, where the $(\nu/a)_{base-ref}$-scale has bearing over the in-plane velocity (viscoelastic), and the other ($\Omega_{\text{sphere}} a$)-scale exerts control over the out-of-plane velocity (inertial).

In the present work, the *hybrid finite element/finite volume scheme* used is an extension of that previously cited in references Belblidia et al. [10, 11]; Wapperom and Webster [12, 13]; Webster et al. [14]. In essence, the numerical solution procedure adopts a time-stepping fractional-staged approach to steady-state, specifically developed and advanced for viscoelastic flow problems. It assumes a Taylor series time expansion and a time-incremental pressure-correction method to derive a semi-implicit scheme implemented over three sub-staged equations per time-step. Spatial discretisation is accomplished via: first, velocity-pressure finite element approximation, on the parent-level quadratic-linear interpolation over the meshed-domain triangulation. This is followed by a cell-vertex stress finite volume approximation on each one of four triangular sub-cells of an individual parent-triangular cell. Thus, the momentum-continuity equations are discretized and solved through this hybrid combination of: semi-implicit Taylor-Galerkin/incremental pressure-correction algorithm (see, for example, Donea [15]; Zienkiewicz et al. [16]; Matallah et al. [17]), together with that of a cell-vertex finite volume sub-cell technique for stress (see, for example, Wapperom and Webster [12, 13]). Over the sub-staged equations per time-step - the first and third are solved through Jacobi iteration, whilst the second invokes a direct Choleski decomposition method. Time-stepping convergence to a steady-state is ensured, from appropriate initial and boundary conditions, through selection of a suitable time-step (here chosen as 10^{-4}) and time-stepping termination criteria. The former must satisfy standard semi-implicit stability criteria, whilst the latter is taken with respect to a relative temporal increment norm over the evolving solution (with a threshold value of 10^{-6}). Fuller detail on these procedures is provided in the references cited above, together with Aboubacar and Webster [18] and Garduño et al. [19].

On mesh convergence Numerical solutions for this complex rotating-sphere problem have been validated through a series of three meshes (Figure 4), displaying relatively gradual refinement, employed to test and quantify solution quality and mesh convergence. The respective meshes are similar in their construction, shape and spatial distribution of elements, only differing in element refinement density over the (r, θ) plane, as detailed in Table 1. The meshes are characterised by two regions, divided and mirrored about the central, 45º-line. As desired, such a procedure captures the detailed flow features, particularly in emerging vortices, whilst achieving sufficient mesh resolution. In this manner, improved definition of vortices has been extracted, specifically for those appearing in regimes beyond second-order. Hence, mesh-convergence is corroborated through these three meshes, confirming consistent trends in vortex evolution. Specifically, the persistent presence of the inertial vortex confirms that this is not a spurious feature, or a consequence of numerical artefacts.

4. Theoretical predictions using the PTT model

First, we note that for *slow-flow* the numerical solutions for the PTT model (Figure 1-bottom row) predict the expected behaviour from the 1960s analytic solutions (see Figure 1-top row). In the case of m=0, the characteristic parabolic Newtonian flow pattern (strictly, Stokesian in the limit of $Re \rightarrow 0$) is recovered, corresponding to the first type of flow (Type 1). This is shown in the left-hand side of Figure 1, where inertia is dominant throughout the entire flow

domain. Central Figure 1 illustrates Type 2 flow structure, which is strongly influenced by elasticity. This pattern contains a secondary flow cell confined near the sphere, and an outer region dominated by inertia. Such a pattern is denoted as *intermediate*. As the value of the *m-parameter* is increased still further, eventually a third flow pattern emerges (Type 3), dominated by viscoelasticity. This third pattern is illustrated in Figure 1, right-hand side. It is important to remark that in Type 1 and Type 2 flows, the streamlines emerge from the poles and gradually migrate towards the equator. Alternatively, in Type 3 flow, the streamlines arise from the equator and shift towards the poles, as can be seen on the right-hand side in Figure 1.

We now move away from the restriction of slow-flow and show that various new flow fields are possible, which do not *necessarily* match any of the experimental pictures in the Giesekus paper [4]. The simulations simply illustrate that there is a plethora of possibilities depending on the flow conditions and the material constants. A similar and related conclusion can of course be drawn from the experiments in the Giesekus paper.

So, we show in Figure 5 numerical predictions for one possible set of variables and two values of the viscosity solvent-fraction parameter β, corresponding to highly-polymeric and high-solvent conditions. The adjustments in polar and equatorial vortices are plain to see. We can of course provide others (see Figures 6-9, for example), but the main object of the present work is to predict the specific appearance of the inertial vortex near the rotating sphere, shown in Figure 2. As such, the PTT model solutions with ($Wi = 0.0210042$, $\varepsilon = 0.04$, ξ=0.0, m=0.14) in Figures 6 and 7 cover Type 2 flow patterns at ever increasing up-scaling of velocity {(Ω_{sphere}, $2.5\,\Omega_{\text{sphere}}$, $5\,\Omega_{\text{sphere}}$); {(3 U_{material}, 10 U_{material}, 100 U_{material})}, for high-solvent (β=0.9) and high-solute fluids (β=1/9), respectively. These solutions indicate the influence of increase in speed. (Please refer back to eq. (8) for the non-dimensional parameter L, and the definition of rotational sphere-speed (Ω_{sphere}) and viscous material velocity scale ($U_{\text{material}} = \nu/a$); then, speed increases are implemented through up-scaling in the boundary conditions). This is amplified somewhat further in Figures 8 and 9a for the high-solvent case alone, where the development of the equatorial vortices is isolated in Figure 9a. In addition, the transition in vortex patterns is highlighted in Figure 9b, covering three different values of rotational speeds. This figure is a clear indication of how the flow structure is strongly dependent on minor changes in sphere rotational-speed.

So, we search for a set of constitutive equation parameters, which will enable us to show that the (elusive) Giesekus inertial vortex can be predicted numerically. This exercise has led to a lengthy search and we show in Figure 10 the nearest we have come to providing the much sought-for numerical solution. As a general observation, the appearance of the elusive equatorial-inertial vortex has only been possible by significant up-scaling of the velocities, specifically via increases in the sphere rotational-speed. One notes the sought-for correspondence to the Giesekus experimental patterns, in both overall flow pattern and structure. The additional shear-thinning characteristics of the PTT model have enabled this solution capture at earlier speed increases than would have been realised with a constant viscosity model, such as the Oldroyd-B model.

5. Conclusions

The general conclusion to be drawn from the work we have undertaken is that many of the experimental pictures in the Giesekus paper are matched in a similar fashion to the numerical predictions. Yet, having said that, we are happy to conclude that, by a suitable choice of the material parameters and flow conditions, it is possible to predict numerically the fascinating appearance of the Giesekus inertial vortex, which has remained a challenge for some workers in the field for over 40 years! Indeed, one of the present authors (KW) specified the prediction of the Giesekus inertial vortex as an unresolved rheological problem in his 2002 Weissenberg Award address.

Acknowledgment

I.E. Garduño gratefully acknowledges financial support from Consejo Nacional de Ciencia y Tecnología (Mexico) through the scholarship No. 310618. The contents of this paper formed part of an Invited Plenary Lecture given by Professor Ken Walters at the ‘Samos’ meeting which honoured the life and on-going scientific career of Professor Roger Tanner.

Appendix I: Contrasting solvent ratios (β) with experimental fluids

Figure AI.1 presents the shear viscosity experimental data for PIB/Decalin, contrasted against the theoretical shear viscosity for LPTT and different solvent ratios (β). Comparing the experimental data from Liang [20] and Hudson [21], it is evident that there is good agreement here. The best match is found for a concentration of 3%. Any departure in agreement, especially for lower concentration (1% - 2%), is probably due to the difference in the temperature used for the measurements taken. This effect is corroborated upon contrasting the close matching between the slope, in the shear-thinning region, for the experimental data from Barnes et al. [22] and the 2% data from Liang et al. [20]; where both measurements were obtained at 25ºC. Regarding the data obtained from Giesekus [23], it may be observed that *they lie closer to the 1% PIB/Decalin from Liang et al.* [20]. This provides surety that the solutions from simulation, for the rotating sphere flow, conducted at $\beta = 0.9$ are well justified. One notes, there is a clear concentration effect in this data, taken from two different sources and at two different temperature levels. Here, as concentration increases from 1% to 5%, gradually the viscosity at 25ºC approaches from below that at 20ºC. At 3% concentration these is almost matching and at 5% there is a flip over of dominance.

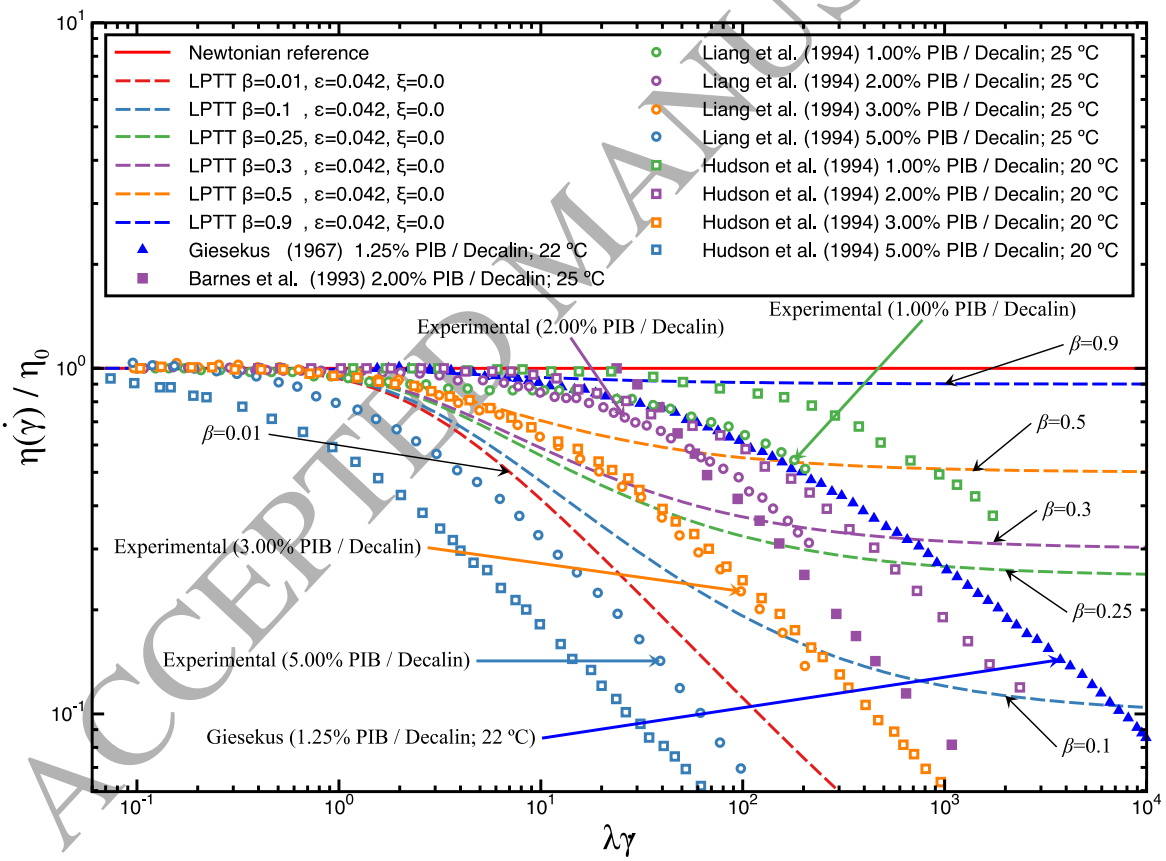

Figure AI.1. Shear viscosity for LPTT ($\beta = [0.01,\ 0.1,\ 0.2,\ 0.3,\ 0.5,\ 0.9]$) compared against experimental data for PIB/Decalin: [1%, 2%, 3%, 5%] PIB/Decalin Liang et al. [20], [1%, 2%, 3%, 5%] PIB/Decalin Hudson et al. [21], 2% PIB/Decalin Barnes et al. [22], 1.25% PIB/Decalin Giesekus [23].

Appendix II: Residuals of the momentum equation

The comparison and contrast through each contribution, made to the momentum equation across the different regimes, is relevant to corroborate satisfaction of the incompressibility condition. The high-solvent viscous-diffusion contributions constitute the largest portion of the total momentum equation temporal-residue, as can be seen in Table II.1. It is seen that the levels for the residues, in the second-order regime, are close to 10^{-7}, whilst in general flow these are about 10^{-6}. As such, these residues can be considered sufficiently small to adequately fulfil the incompressibility condition.

Table II.1. Temporal L2-norm residues, momentum equation various component contributions; LPTT, across flow regimes, $\beta = 0.9$

		Outside second-order regime
Component	Second order	General flow
$\lvert\nabla \cdot T\rvert$	0.282×10^{-7}	0.148×10^{-4}
$\lvert\nabla \cdot \tau\rvert$	0.325×10^{-8}	0.737×10^{-5}
$\lvert\nabla \cdot 2\mu_s d\rvert$	0.271×10^{-7}	0.158×10^{-4}
$\lvert u \cdot \nabla u\rvert$	0.939×10^{-9}	0.534×10^{-5}
$\lvert\nabla p\rvert$	0.724×10^{-10}	0.137×10^{-4}
$\lvert$all comp$\rvert$	0.267×10^{-7}	0.384×10^{-6}

References

[1] D.V. Boger, K. Walters, Rheological Phenomena in Focus, Elsevier, Amsterdam, 1993.

[2] R.H. Thomas, K. Walters, The motion of an elastico-viscous liquid due to a sphere rotating about its diameter, The Quarterly Journal of Mechanics and Applied Mathematics. 17 (1964) 39-53.

[3] K. Walters, J.G. Savins, A rotating-sphere elastoviscometer, J. Rheology. 9 (1965) 407-416.

[4] H. Giesekus, Mass and heat transfer at low flow of viscoelastic fluids around a rotating sphere, Rheologica Acta. 9 (1970) 30-38.

[5] K. Walters, N.D. Waters, The interpretation of experimental results obtained from a rotating-sphere elastoviscometer, British Journal of Applied Physics. 15 (1964) 989-991.

[6] B.D. Coleman, W. Noll, An approximation theorem for functionals, with applications in continuum mechanics, in: The Foundations of Mechanics and Thermodynamics, Springer Berlin Heidelberg, Berlin, Heidelberg, 1974: pp. 97-112.

[7] R.L. Fosdick, B. Kao, Steady flow of a simple fluid around a rotating sphere, Rheologica Acta. 19 (1980) 675-697.

[8] R.W. Williams, On the secondary flow induced by spheres and discs rotating in elastic-viscous liquids, Rheologica Acta 19 (1980) 548-573.

[9] N. Phan-Thien, R.I. Tanner, A new constitutive equation derived from network theory, Journal of Non-Newtonian Fluid Mechanics. 2 (1977) 353-365.

[10] F. Belblidia, H. Matallah, B. Puangkird, M.F. Webster, Alternative subcell discretisations for viscoelastic flow: Stress interpolation, Journal of Non-Newtonian Fluid Mechanics. 146 (2007) 59-78.

[11] F. Belblidia, H. Matallah, M.F. Webster, Alternative subcell discretisations for viscoelastic flow: Velocity-gradient approximation, Journal of Non-Newtonian Fluid Mechanics. 151 (2008) 69-88.

[12] P. Wapperom, M.F. Webster, A second-order hybrid finite-element/volume method for viscoelastic flows, Journal of Non-Newtonian Fluid Mechanics. 79 (1998) 405-431.

[13] P. Wapperom, M.F. Webster, Simulation for viscoelastic flow by a finite volume/element method, Comp. Meth. Appl. Mech. Eng. 180 (1999) 281-304.

[14] M.F. Webster, H.R. Tamaddon-Jahromi, M. Aboubacar, Time-dependent algorithm for viscoelastic flow-finite element/volume schemes, Num. Meth. Partial Diff. Equ. 21 (2005) 272-296.

[15] J. Donea, Taylor-Galerkin method for convective transport problems, Int. J. Num. Meth. Eng. 20 (1984) 101-119.

[16] O.C. Zienkiewicz, K. Morgan, J. Peraire, M. Vandati, R. Löhner, Finite elements for compressible gas flow and similar systems, 7th Int. Conf. Comput. Meth. Appl. Sci. Eng. Versailles, France (1985).

[17] H. Matallah, P. Townsend, M.F. Webster, Recovery and stress-splitting schemes for viscoelastic flows, Journal of Non-Newtonian Fluid Mechanics. 75 (1998) 139-166.

[18] M. Aboubacar, M.F. Webster, A cell-vertex finite volume/element method on triangles for abrupt contraction viscoelastic flows, Journal of Non-Newtonian Fluid Mechanics. 98 (2001) 83-106.

[19] I.E. Garduño, H.R. Tamaddon-Jahromi, M.F. Webster, Oldroyd-B numerical solutions about a rotating sphere at low Reynolds number, Rheologica Acta. 54 (2015) 235-251.

[20] R.F. Liang, M.R. Mackley, Rheological characterization of the time and strain dependence for polyisobutylene solutions, Journal of Non-Newtonian Fluid Mechanics. 52 (1994) 387–405.

[21] N.E. Hudson, J. Ferguson, The anomalous shear flow properties of S1, Journal of Non-Newtonian Fluid Mechanics. 52 (1994) 105–119.
[22] H.A. Barnes, J.F. Hutton, K. Walters, An Introduction to Rheology, Third ed., Elsevier, Amsterdam, 1993.
[23] H. Giesekus, The secondary flow in a cone-plate configuration: dependence on the rotational speed for various polymer systems, Rheologica Acta. 6 (1967) 339–353.
[24] K. Walters, Rheometry, Chapman and Hall, London, 1975.

Table 1. Mesh characteristics: coarse (M1), medium (M2), refined (M3) meshes

Mesh	M1	M2	M3
Total nodes	2501	4941	7381
Total elements	1200	2400	3600
Total boundary nodes	200	280	360
Degrees of freedom	15657	30917	46177
Aspect ratio (Sphere radius: ext. radius)	1:20	1:20	1:20

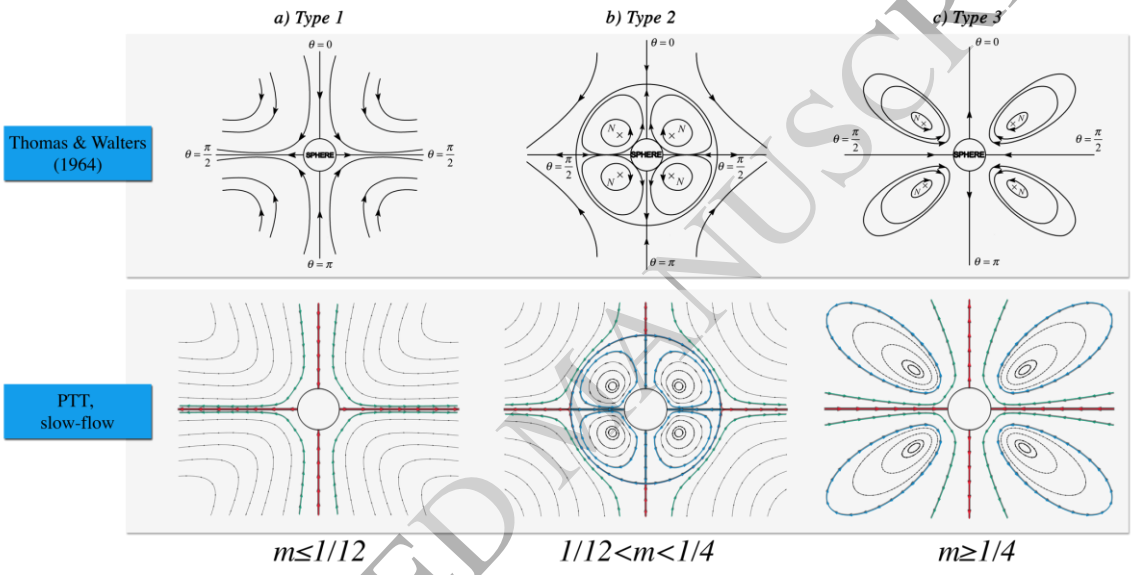

Figure 1. Second-order slow-flow regime: types of flow patterns. Upper-row, theoretical results from Thomas and Walters [2]. Bottom-row, PTT model numerical solutions.

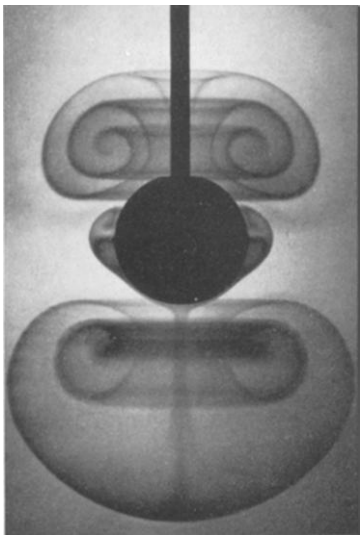

Figure 2. Giesekus [4] experimental picture for 1.3% solution of polyisobutylene in decalin, $\Omega_{\text{sphere}} = 150\ \text{min}^{-1}$.

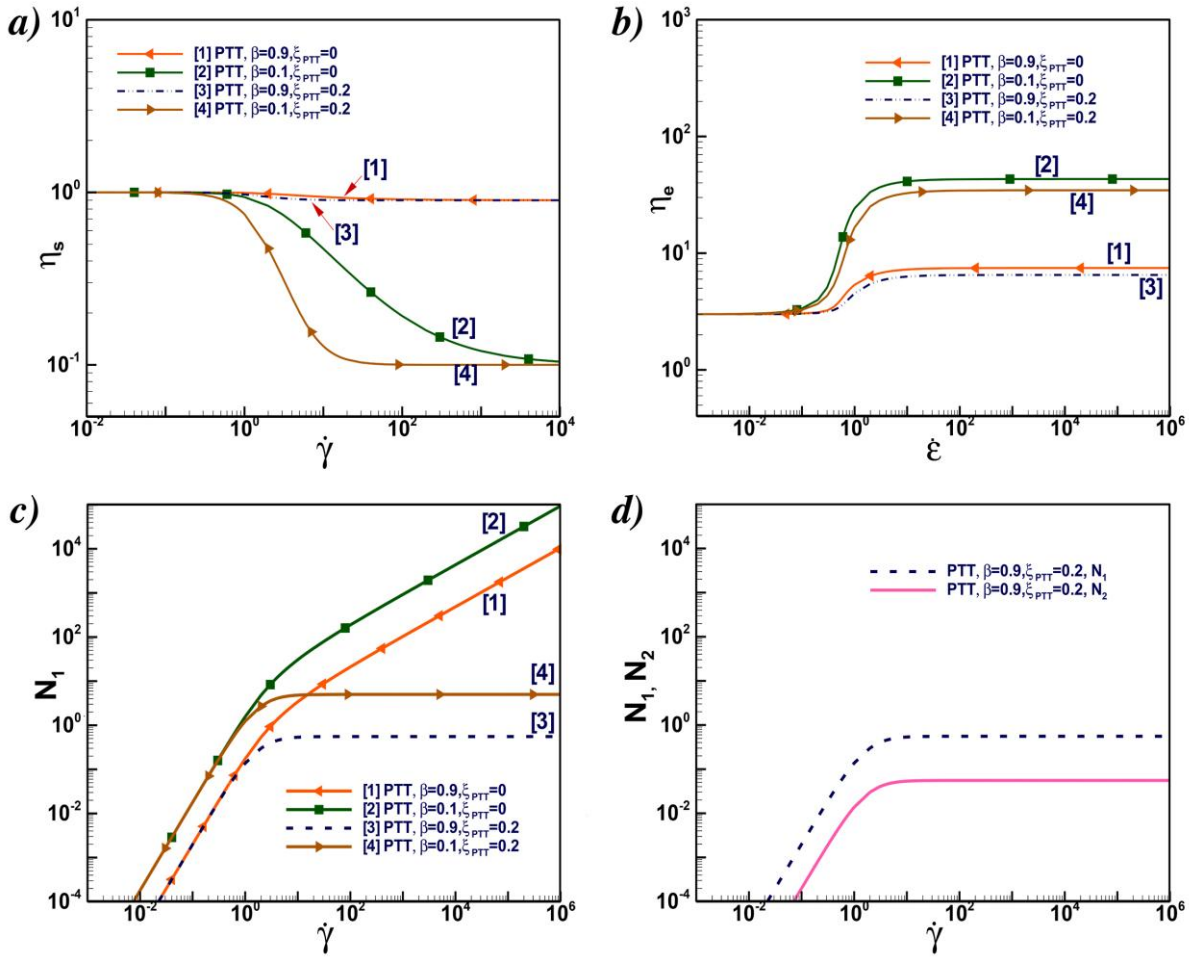

Figure 3. Material functions for PTT model ($\varepsilon = 0.04$, ξ=0.0, 0.2), β=0.9, 0.1;
a) shear viscosity, b) extensional viscosity, c) first normal stress-difference,
d) second normal stress-difference.

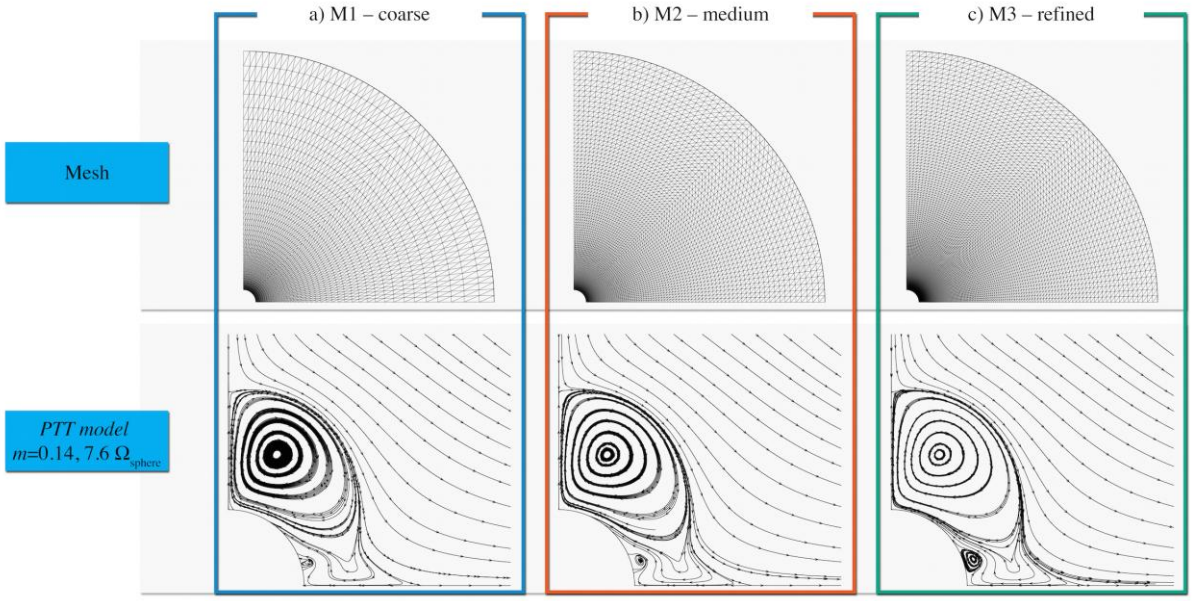

Figure 4. Upper-row, finite element meshes: a) M1 - coarse b) M2 - medium c) M3 - refined; Bottom-row numerical solutions for respective meshes; PTT model ($Wi = 0.021,\ \varepsilon = 0.04,\ \xi = 0.0$).

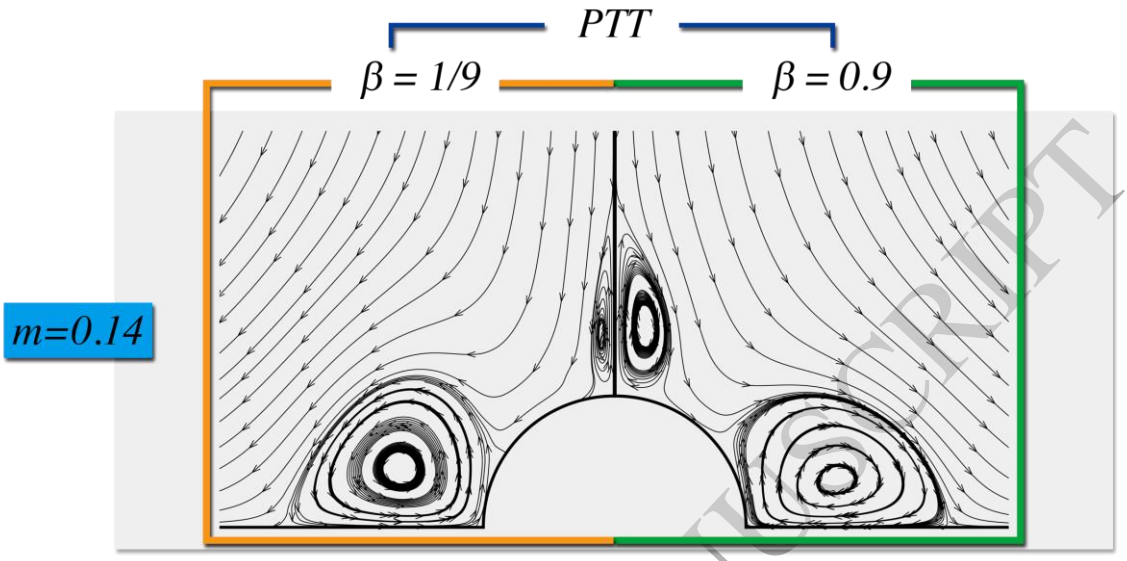

Figure 5. Flow patterns for a PTT model ($Wi = 0.021,\ \varepsilon = 0.04,\ \xi$=0.0): solvent ratio ($\beta$) effects, high solute ($\beta$=1/9) and high solvent ($\beta$=0.9); base case {$m$=0.14}.

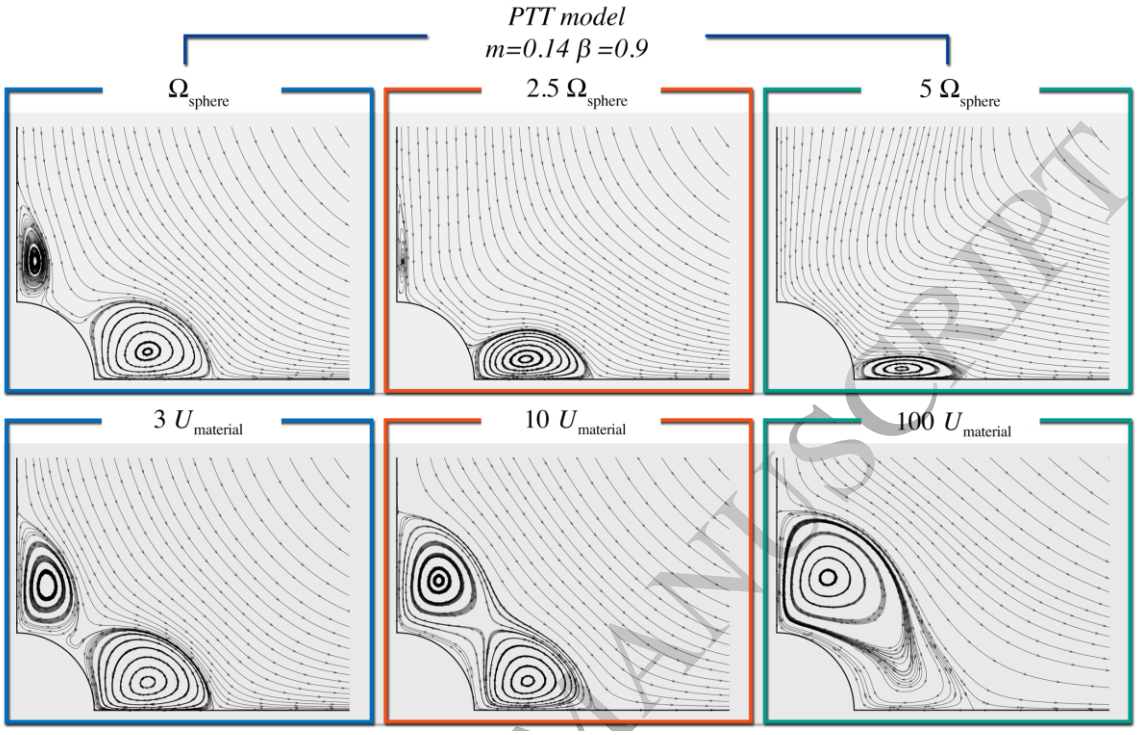

Figure 6. Flow patterns, high-solvent: increasing sphere-velocity scaling and decreasing viscous-velocity scaling, with PTT model constants: $Wi = 0.021$, $\varepsilon = 0.04$, ξ=0.0, m=0.14, β=0.9.

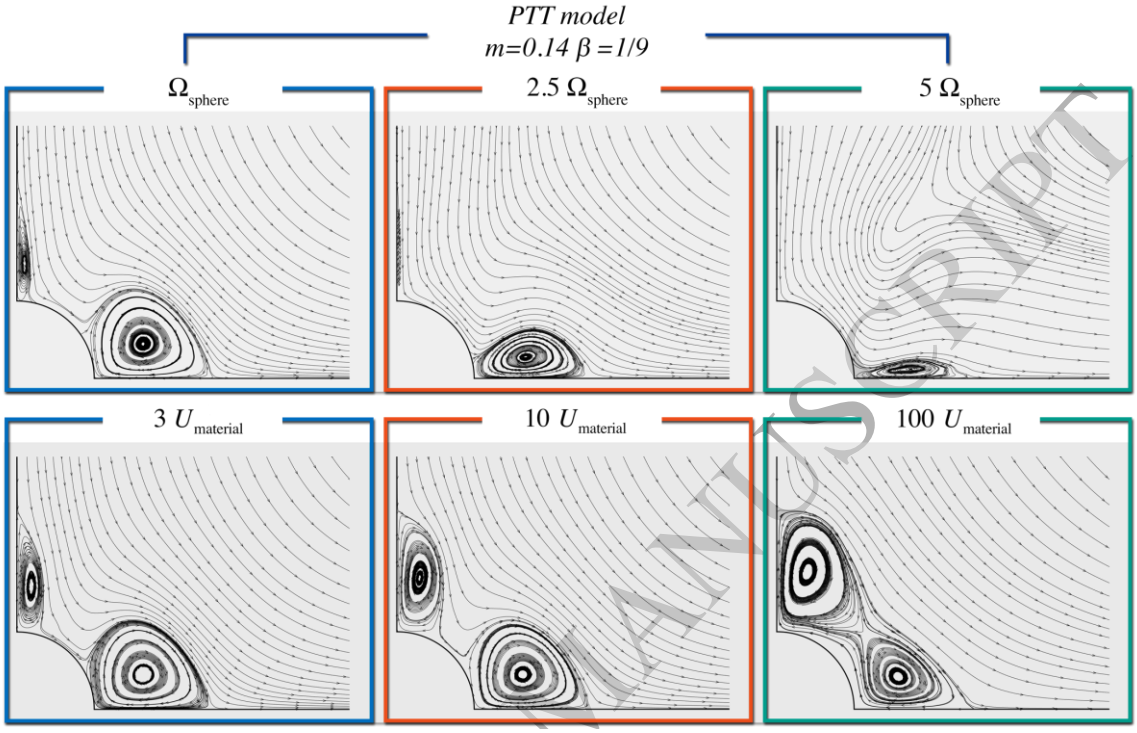

Figure 7. Flow patterns, low-solvent: increasing sphere-velocity scaling and decreasing viscous-velocity scaling, with PTT model constants: $Wi = 0.021$, $\varepsilon = 0.04$, ξ=0.0, m=0.14, β=1/9.

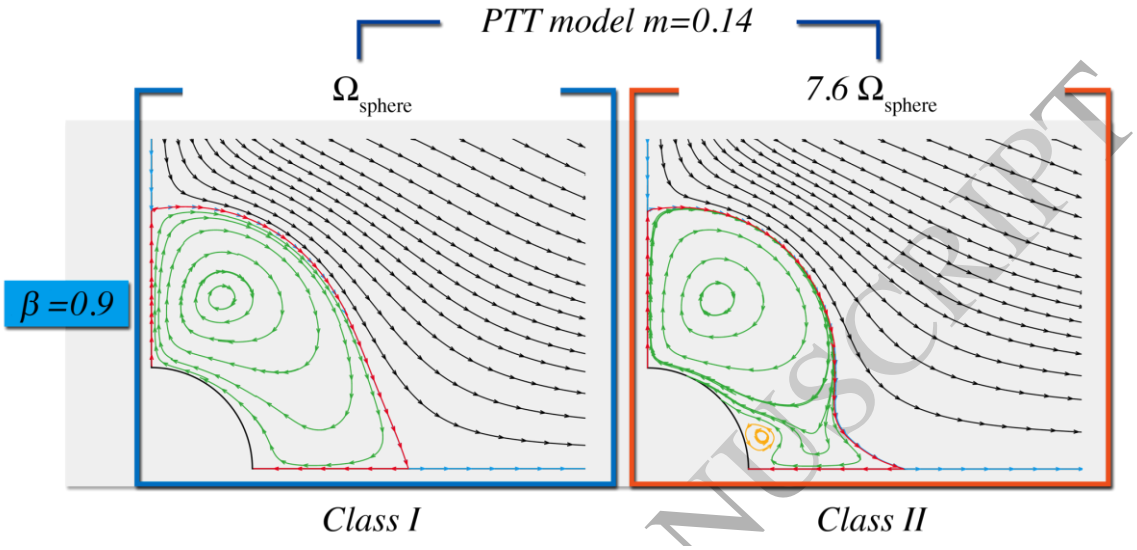

Figure 8. Possible alternative classes of solutions with increasing sphere speed, 1000 U_{material}; with PTT model constants: $Wi = 0.021$, $\varepsilon = 0.04$, ξ=0.0.

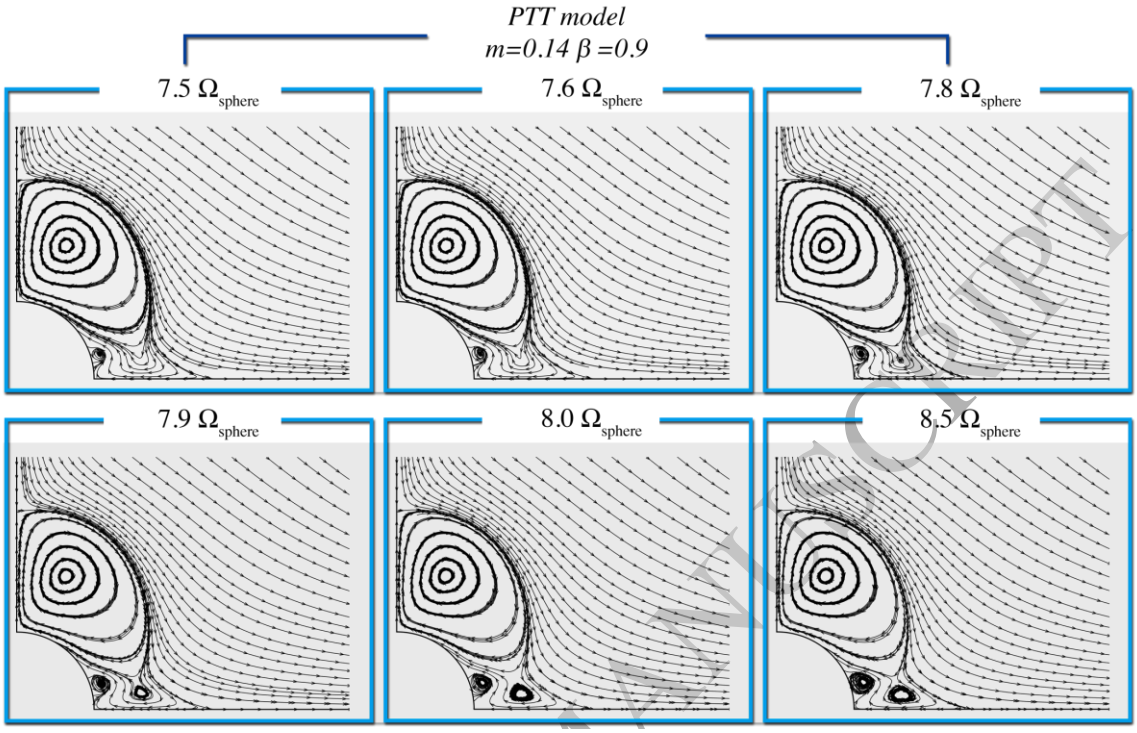

Figure 9a. Development of equatorial vortices, for PTT model constants:
$Wi = 0.021,\ \varepsilon = 0.04,\ \xi$=0.0, m=0.14, β=0.9; 1000 U_{material}, high-solvent solutions.

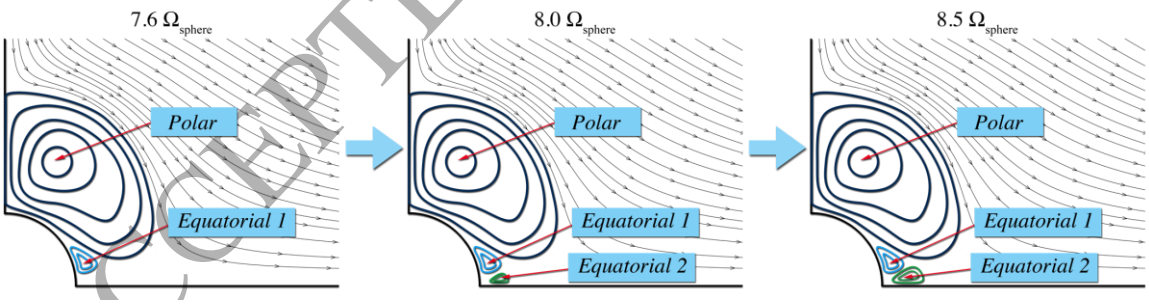

Figure 9b. Vortex evolution {m=0.14, β=0.9, 1000 U_{material}}, various rotational speeds, with PTT model constants: $Wi = 0.021,\ \varepsilon = 0.04,\ \xi$=0.0.

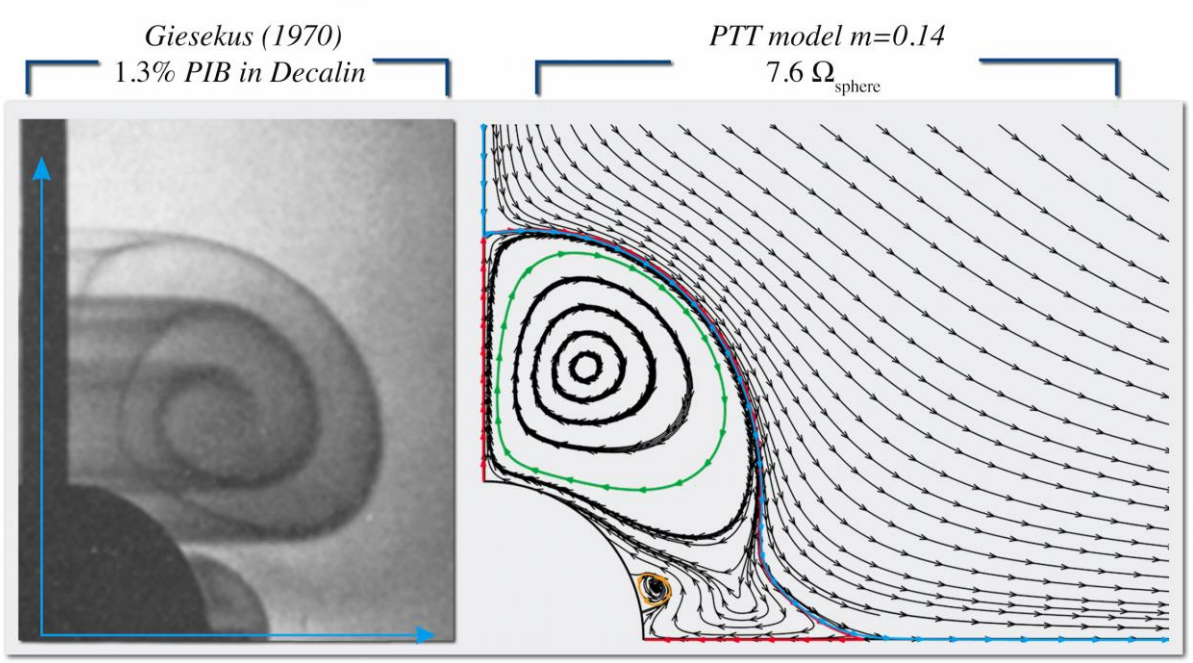

Superimposed

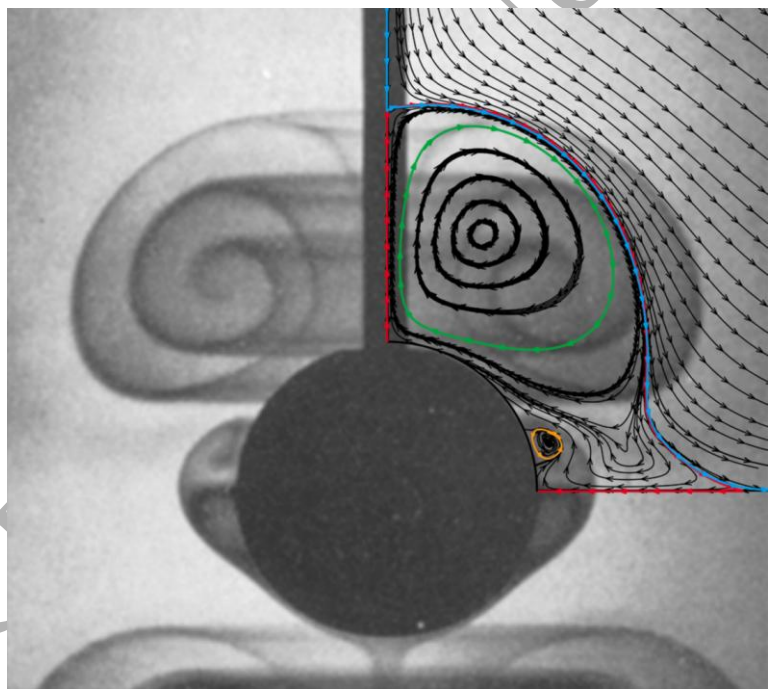

Figure 10. Best matching solution: Top: rhs PTT model constants {m=0.14, β=0.9, 7.6 Ω_{sphere}, 1000 U_{material}, $Wi = 0.021$, $\varepsilon = 0.04$, ξ=0.0 }; lhs Giesekus [4] experimental findings for 1.3% PIB in Decalin. Bottom: Superimposing numerical results with the Giesekus [4] experimental picture.